A survey of 286 Virgo cluster galaxies at optical *griz* and near-IR *H* band: surface brightness profiles and bulge–disc decompositions

Michael McDonald,[1]★ Stéphane Courteau,[2]★ R. Brent Tully[3]★ and Joel Roediger[2]★

[1]*Department of Astronomy, University of Maryland, College Park, MD 20742-2421, USA*
[2]*Department of Physics, Engineering Physics and Astronomy, Queen's University, Kingston, ON K7L 3N6, Canada*
[3]*Institute for Astronomy, University of Hawaii, 2680 Woodlawn Drive, Honolulu, HI 96822, USA*

ABSTRACT

We present and *g*-, *r*-, *i*-, *z*- and *H*-band surface brightness profiles and bulge–disc decompositions for a morphologically broad sample of 286 Virgo Cluster Catalogue (VCC) galaxies. The *H*-band data come from a variety of sources including our survey of 171 VCC galaxies at the University of Hawaii (UH) 2.2-m telescope, Canada–France–Hawaii Telescope (CFHT) and United Kingdom Infrared Telescope (UKIRT), and another 115 galaxies from the Two Micron All Sky Survey (2MASS) and GOLDMine archives. The optical data for all 286 VCC galaxies were extracted from the Sloan Digital Sky Survey (SDSS) images. The *H*-band and the SDSS *griz* data were analysed in a homogeneous manner using our own software, yielding a consistent set of deep, multiband surface brightness profiles for each galaxy. Average surface brightness profiles per morphological bin were created in order to characterize the variety of galaxy light profiles across the Hubble sequence. The 1D bulge–disc decomposition parameters, as well as non-parametric galaxy measures, such as effective radius, effective surface brightness and light concentration, are presented for all 286 VCC galaxies in each of the five optical/near-infrared wavebands. The profile decompositions account for bulge and disc components, spiral arms, nucleus and atmospheric blurring. The Virgo spiral galaxy bulges typically have a Sérsic index $n \sim 1$, while elliptical galaxies prefer $n \sim 2$. No galaxy spheroid requires $n > 3$. The light profiles for 70 per cent of the Virgo elliptical galaxies reveal the presence of both a spheroid and disc component. A more in-depth discussion of the structural parameter trends can be found in McDonald, Courteau & Tully. The data provided here should serve as a base for studies of galaxy structure and stellar populations in the cluster environment. The galaxy light profiles and bulge–disc decomposition results are available at the Centre de Données astronomiques de Strasbourg (CDS; http://http://cds.u-strasbg.fr/) and the author's own website (http://www.astro.queensu.ca/virgo).

Key words: surveys – galaxies: clusters: individual: Virgo – galaxies: fundamental parameters – galaxies: general – galaxies: photometry – galaxies: structure.

1 INTRODUCTION

The advent of large-area near-infrared (NIR) surveys such as the Two Micron All Sky Survey (2MASS; Skrutskie et al. 2006) and the United Kingdom Infrared Telescope (UKIRT) Infrared Deep Sky Survey (UKIDSS; Lawrence et al. 2007) has forever improved our understanding of galaxy structure and evolution. The NIR data provide an unobscured view of galaxy structure, due to the relative insensitivity of NIR light to dust extinction, while probing the oldest and most representative stellar populations by mass. Unfor-

tunately, the aforementioned surveys, designed largely for the study of bright infrared sources, use short exposure times (7.8 and 40 s for the 2MASS and the UKIDSS, respectively) and suffer from the tremendous brightness of the NIR sky (typically ∼3 orders of magnitude brighter than at *r* band), leading to rather shallow surface brightness (SB) limits for galaxy studies when compared to similarly designed optical surveys.

The stability of the optical night sky, especially at *r* and *i* bands, allows for deep, accurate optical surface photometry with relatively short integrations and careful data processing. The Sloan Digital Sky Survey (SDSS; Adelman-McCarthy et al. 2008) has revolutionized optical astronomy, increasing the wealth of available astronomical data (both photometric and spectroscopic) by orders of magnitude. A development made possible by the SDSS was the unraveling

★E-mail: mcdonald@astro.umd.edu (MM); courteau@astro.queensu.ca (SC); tully@ifa.hawaii.edu (RBT); jroediger@astro.queensu.ca (JR)

of bimodalities in various galaxy properties such as colour, star formation rate and clustering (e.g. Strateva et al. 2001; Blanton et al. 2003; Kauffmann et al. 2003; Baldry et al. 2004; Balogh et al. 2004; Brinchmann et al. 2004). These and other studies have provided firm evidence that galaxies can be separated into two distinct classes: blue, star-forming galaxies found primarily in the field and red, quiescent galaxies found primarily in clusters.

Prior to these findings, Tully & Verheijen (1997; hereafter TV97) reported a different form of galaxy structural bimodality. This one, independent of the SDSS colour bimodality, was based on a sample of 62 members of the Ursa Major (UMa) cluster of galaxies; TV97 found a bimodal distribution in the distribution of K'-band (2.2 μm) SB of galaxy discs. McDonald, Courteau & Tully (2009a), who reanalysed the same UMa data using more sophisticated light profile decompositions to measure the disc structural parameters, corroborated TV97's results. Bell & de Blok (2000) have, however, argued that the UMa sample was too small for a statistically significant proof of bimodality. It is partly this unresolved issue, as well as the need for a complete NIR survey of a nearby galaxy cluster to study the (dust-free) structural parameters and stellar populations of cluster galaxies, that motivated our NIR survey of the Virgo cluster.

Using the optical and NIR data presented in this paper, McDonald et al. (2009b) performed 1D bulge–disc decompositions for 286 Virgo cluster galaxy SB profiles and bolstered the evidence for a disc SB bimodality. Furthermore, it was found, for galaxies of all morphologies, that the *effective* SB (defined as the SB measured at the half-light radius) distribution had three peaks, each defining (i) high SB (HSB), gas-poor galaxies, (ii) low SB, gas-poor galaxies and HSB, gas-rich galaxies and (iii) low SB, gas-rich galaxies. A more thorough discussion of these, and other results from this survey, can be found in McDonald et al. (2009b).

This paper presents the deep, optical and NIR SB profiles for our sample of 286 Virgo cluster galaxies. The paper outline is as follows. We describe in Section 2 the sample selection and the optical and NIR data acquisition. In Section 3, we give an overview of our NIR data reduction methods, and we describe in Section 4 the process of SB profile extraction for both the optical and NIR data. We discuss in Section 5 the quality of the NIR data and compare our data products with those from the 2MASS and the SDSS. The full collection of SB profiles is presented in Section 6, along with a brief analysis of the average profile shape for various galaxy types. Galaxy structural parameters from our light profile decompositions and from non-parametric galaxy measurements are presented in Section 7. We conclude and ponder future work in Section 8.

In this paper, we assume a distance of 16.5 Mpc or $m - M = 31.18$ for all Virgo cluster galaxies (Mei et al. 2007). At that distance, 1 arcsec equals 80 pc.

2 VIRGO SAMPLE

The construction of an unbiased distribution of galaxy SB requires volume completeness, which can be most easily obtained for galaxies in a cluster which all lie at a common distance. Our sample is drawn from the Virgo Cluster Catalogue of Binggeli, Sandage & Tammann (VCC; 1985). The VCC catalogue contains 2096 galaxies within an area of $\sim$140 deg^2 on the sky, centred on the galaxy M87 at $\alpha \sim 12^{\rm h}25^{\rm m}$ and $\delta \sim 13°$. The VCC is asserted to be complete down to a limiting absolute magnitude of $M_B \sim -13$ and to contain many objects as faint as $M_B \sim -11$. The full sample was reduced to a manageable size of 286 galaxies by performing a brightness cut ($M_B \leq -15.15$ mag), a spatial cut (to remove contamination from W, W' and M background groups;

Sandage, Binggeli & Tammann 1985) and a velocity cut ($V_{\rm rad} < 3000\,{\rm km\,s^{-1}}$). These cuts, which yield a sample covering a wide range of luminosities and morphologies, are discussed in further detail in McDonald et al. (2009b).

2.1 NIR Data

Deep H-band imaging for some VCC galaxies is already available from the 2MASS and GOLDMine[1] (Gavazzi et al. 2003) data bases. H-band images from GOLDMine were kindly provided by G. Gavazzi, while calibrated 2MASS galaxy images were extracted from the online data base. Many of the 2MASS and GOLDMine images were not deep enough for our purposes. Whilst adequate for large HSB galaxies, the high 2MASS SB threshold (typically $\mu_H = 21$ mag arcsec^{-2} – Bell et al. 2003; Courteau et al. 2007; Kirby et al. 2008) undermines the use of that data base for deep extragalactic studies. Likewise, only a fraction of the available GOLDMine images were deep enough to properly separate bulge and disc light components, or suffered from ghost images. Whenever possible, we attempted to salvage such images by either masking the ghosts or confining our analysis to a single chip, which were typically unaffected by contamination due to ghosts. We secured H-band imaging for the remainder (187 galaxies) of our sample with the detectors Ultra Low Background Camera (ULBCam, UH 2.2-m telescope), Wide Field Camera (WFCAM) (UKIRT) and Wide-field Infrared Camera (WIRCAM) [Canada–France–Hawaii Telescope(CFHT)] over the period 2005–09. The existing and new observations are summarized in table 1 of McDonald et al. (2009b).

The SB profiles for the deep GOLDMine and 2MASS images were measured using the same techniques as our new NIR images to ensure uniformity for the entire data base. Further details regarding the data reduction process and quality are given below.

2.2 Optical data

We have extracted calibrated *ugriz* images from the SDSS for the 286 VCC galaxies in our sample. SB profiles and total luminosities were extracted for all of these galaxies in all five SDSS bands using procedures described in Courteau (1996) and McDonald et al. (2009b). *u*-band images were consistently shallower than those in the *griz* bands and, thus, were discarded. Sky levels for background subtraction and the photometric zero-points for calibration were obtained from the SDSS image headers and the SDSS archives, respectively. However, we will see in Section 4.1 that we ultimately prefer our own estimates of the sky background for each of the galaxy images. The remainder of the profile extraction technique is identical to that used for the NIR photometry, as we describe below.

3 NIR OBSERVATIONS AND DATA REDUCTION

Virgo cluster galaxies which lacked suitable NIR imaging were observed with ULBCam[2] on the 2.2-m UH telescope (Hall et al. 2004), WIRCAM on the 3.6-m CFHT (Puget et al. 2004) and WFCAM on the 3.8-m UKIRT (Hambly et al. 2008) from 2005 April to 2008 May (see table 1 of McDonald et al. 2009b).

For all three NIR imagers, we only used one of the available detectors given the relatively small size of our targets. A single UL-BCam detector has a $8.5 \times 8.5 \, \text{arcmin}^2$ field of view (FOV) with a pixel scale of $0.25 \, \text{arcsec pixel}^{-1}$, while WFCAM has a $13.6 \times 13.6 \, \text{arcmin}^2$ FOV with a pixel scale of $0.40 \, \text{arcsec pixel}^{-1}$ and WIRCAM has a $10.2 \times 10.2 \, \text{arcmin}^2$ FOV with a pixel scale of $0.30 \, \text{arcsec pixel}^{-1}$. Altogether, 129, 35 and 27 galaxies were observed at H band with ULBCam, WIRCAM and WFCAM, respectively.

Given the rapid NIR sky fluctuations, we used a maximum single frame exposure time of 40 s with ULBCam, 15 s with WIRCAM and 10 s with WFCAM to maximize sky flux, while keeping within the detector's linear regime. A dithering script was used to minimize
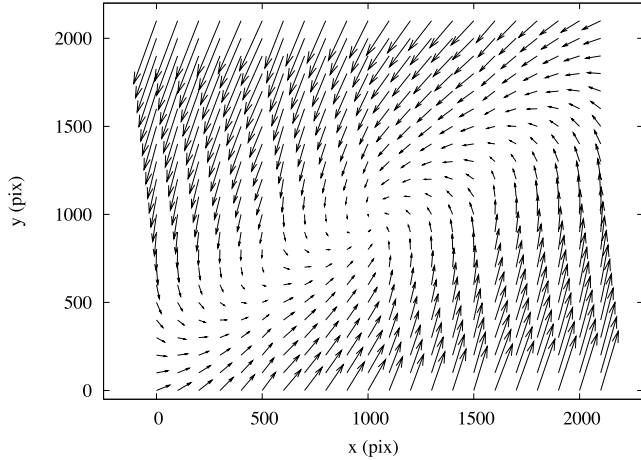

Figure 1. Geometric distortion in one array of the ULBCam 4096×4096 detector. The magnitudes of the vectors have been increased by a factor of 8 for clarity.
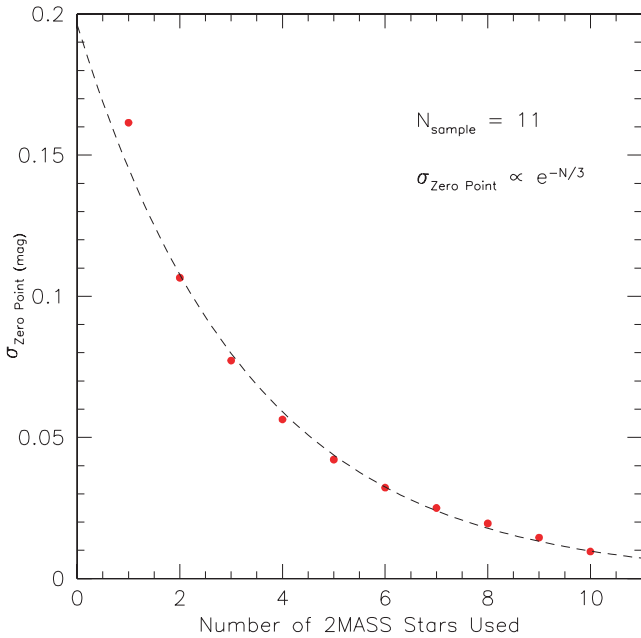

Figure 2. Calibration error as a function of the number of field stars used per calibration. In order to compute the standard deviation, N stars were chosen at random and the mean brightness was computed. This process was repeated 10 000 times to ensure every possible combination of stars was used. The standard deviation represents the difference in means depending on which N out of 11 stars were chosen.

resampling of bad pixels. In order to ensure sampling of each galaxy out to several effective radii, we first pre-classified the galaxies by eye as high, medium and low SB. For these three classes, we aimed for total exposure times of 8, 16 and 24 min (on the 2.2-m UH telescope), respectively. These different exposure times were
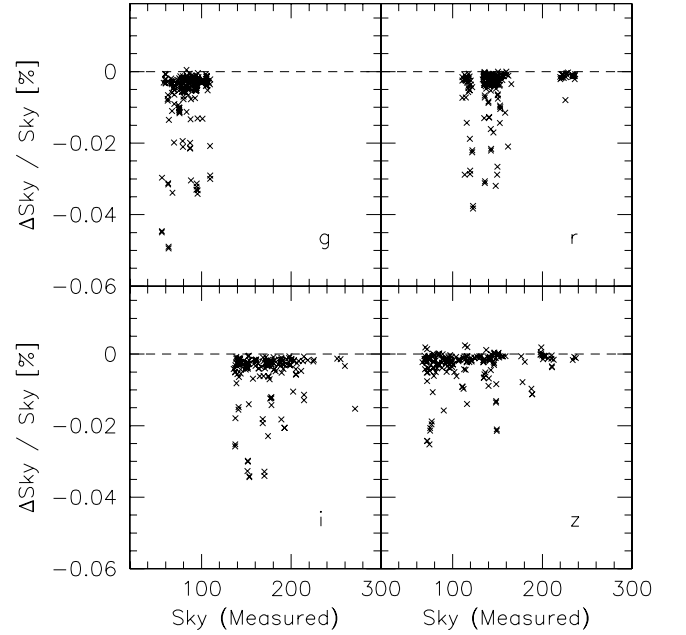

Figure 3. Difference between our interactively measured and the SDSS-provided sky flux as a function of our measured sky level (in counts). Negative Y-values indicate a larger SDSS value.
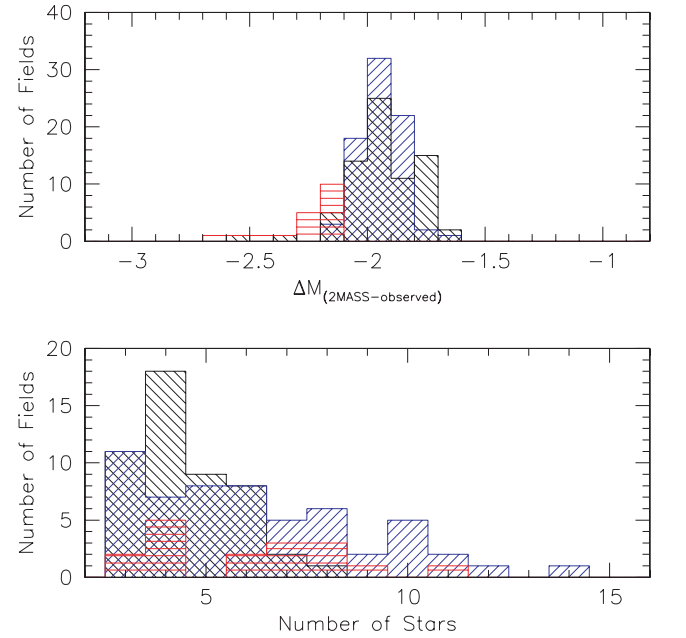

Figure 4. Upper panel: distribution of magnitude offsets between observed and 2MASS measurements for foreground stars over many observing runs. The black, red and blue histograms correspond to observations taken in 2005, 2006 and 2007, respectively. Lower panel: number of foreground stars used to determine a relative magnitude offset per single observation; a minimum of three stars per field was found to be necessary to constrain the photometric zero-point.
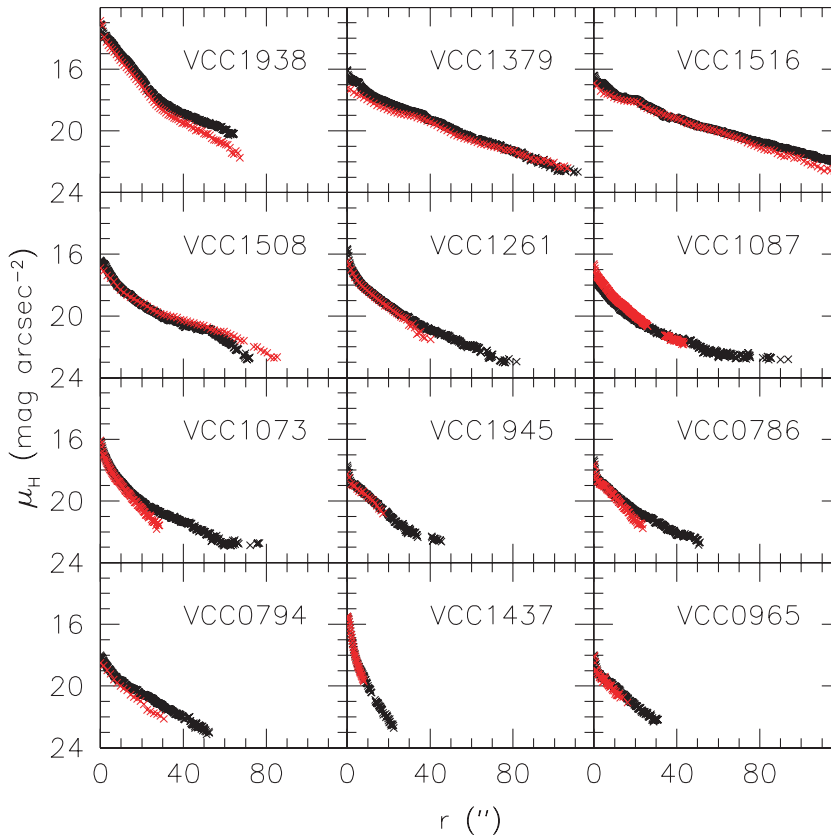
Figure 5. Comparison of GOLDMine (red) and ULBCam (black) *H*-band SB profiles for a sample of matching galaxies, ordered (from left to right and top to bottom) by total luminosity. The good match in profile depth found at the bright end of the sample is lost for fainter galaxies.

motivated by our desire for a well-sampled disc in order to obtain a reliable bulge–disc decomposition.

Basic flat-fielding, stacking and bad pixel rejection procedures were applied to the ULBCam data using the XVISTA astronomical software package.[3] Primary data reductions for the WIRCAM and WFCAM made use of observatory pipelines. The removal of geometric distortion and photometric calibration of the ULBCam data, as well as the procedures for extraction of SB profiles for all NIR and optical data, are described below.

3.1 ULBCam geometric distortion

We corrected the significant geometric distortions in ULBCam images by observing the dense star field FS17 and computing the offset between the predicted and observed stellar positions, following Meurer et al. (2002). The following simple correction minimizes the distortion in our images:

$$\Delta x(\text{pixel}) = 16.64 - 0.0162y,$$

$$\Delta y(\text{pixel}) = 0.0182x - 0.0230y + 3.80.$$

Additionally, each ULBCam 2048×2048 detector is comprised of four smaller 512×2048 arrays that required horizontal offsets of -4 pixels (arrays 1 and 3) to account for their physical separation prior to determining the detector-wide astrometric correction. The 2D pattern of this correction model, shown in Fig. 1, is accurate to within 1 pixel (0.25 arcsec) across the full FOV.

[3] http://astronomy.nmsu.edu/holtz/xvista/index.html

3.2 NIR flux calibration

The target flux calibration is based on 2MASS foreground stars. For each galaxy field, all stars above a given flux level (corresponding to the minimum detection level in 2MASS) were marked and their coordinates cross-correlated with the 2MASS stellar library. Typically, three to seven 2MASS stars per ULBCam galaxy field were marked. The ratio of our instrumental magnitudes for those stars to those provided by 2MASS enabled a calibration of all of our photometry at each pixel, independent of any airmass or photometric variations (our NIR images were still all obtained in most favourable conditions). This approach was tested extensively against the traditional method of multiple standard star observations per night and found to be equally reliable provided that at least three 2MASS stars were used per field. Under such conditions, the standard deviation of the derived zero-point corrections from each star is ∼0.1 mag, as seen in Fig. 2. This error is comparable to those quoted for NIR photometric calibrations using standard star fields (de Jong 1996; Gavazzi et al. 1996; MacArthur, Courteau & Holtzman 2003).

4 SURFACE BRIGHTNESS PROFILE EXTRACTION

The measurements of galaxy SBs rely on the careful mapping, in one or two dimensions, of a representative light profile. Our profile extraction uses numerous XVISTA routines and procedures described in Courteau (1996). We review the important steps below. While azimuthally averaged SB profiles for some of our galaxies are available elsewhere (e.g. 2MASS and GOLDMine), we have recovered original images in all cases and rederived our own SB

profiles for all of these galaxies to ensure a homogeneous data base.

4.1 Sky measurement

A sky level error of only ± 0.01 per cent at NIR wavelengths can result in either an artificial truncation (oversubtraction) or upturn (undersubtraction) of the galaxy SB profile at large radii. At H band, this truncation/upturn would occur at ~ 23.5 mag arcsec^{-2}. An accurate assessment of the sky level is thus crucial for the extraction of a reliable, deep, NIR SB profile.

For all images, the sky level is estimated in the final fully reduced image by isolating five regions (by eye) away from the galaxy, free of any other sources, and by calculating the mode of the sky intensities per pixel within each sky region. The average and standard deviation of the five sky values were then computed. Sky levels were estimated this way not only for our data, but also for 2MASS and GOLDMine images. The typical sky fluctuation for our NIR data is ~ 0.005 per cent.

Thanks to its extended sky coverage, SDSS should achieve accurate sky level measurements (http://www.sdss.org/dr5/algorithms/flat_field.html). However, we still use our interactive assessment of the sky background, as described above, for all SDSS data. Fig. 3 shows the difference between our measured sky values and those provided by SDSS. The latter is always biased high, likely due to the inclusion of bright, extended sources. Our interactive technique ensures a (mostly) contaminant-free selection of sky fields. However, due to the fact that we extend the SB profiles to the edge of the FOV, the uncertainty in the profile shape is dominated by systematic (sky measurement) errors at large radii. While seemingly small, sky level

errors of ~ 0.02–0.04 per cent, as seen in Fig. 3, yield significant deviations in a galaxy SB profile (McDonald et al. 2009b). We find that the shape of the SB profile in g band is typically dominated by sky measurement errors by $\mu_g \sim 26$ mag arcsec^{-2}. Below this SB level (and corresponding SBs in r, i, z), users should consider the data with 1σ sky error envelopes.

4.2 PSF measurement and star masking

The seeing point spread function (PSF) is often modelled either as a Gaussian or a Moffat (1969) function. The latter has broader wings, which better matches our stellar fields; we have thus used the Moffat function throughout our analysis. On average, 17 stars per field were modelled for PSF measurements. The average full width at half-maximum (FWHM) for all ULBCam observations taken over 2005–08 was 1.2 ± 0.2 arcsec; slightly better imaging was achieved at CFHT and UKIRT. The average FWHM measurement for each image is later used to convolve the analytical models for the galaxy bulge and disc light (see McDonald et al. 2009a).

The identification of foreground stars also enables their removal from the galaxy light. The use of circular masks with radii equal to $4 \times$ FWHM ensures that most of this contaminant light is properly removed. Our automated masking routine could not identify bright stars with diffraction spikes or other irregularly shaped features; those obtrusive objects were manually masked.

4.3 Isophotal fitting

SB profiles were extracted for all of our galaxy images. The XVISTA command, PROFILE, performs this operation through isophotal

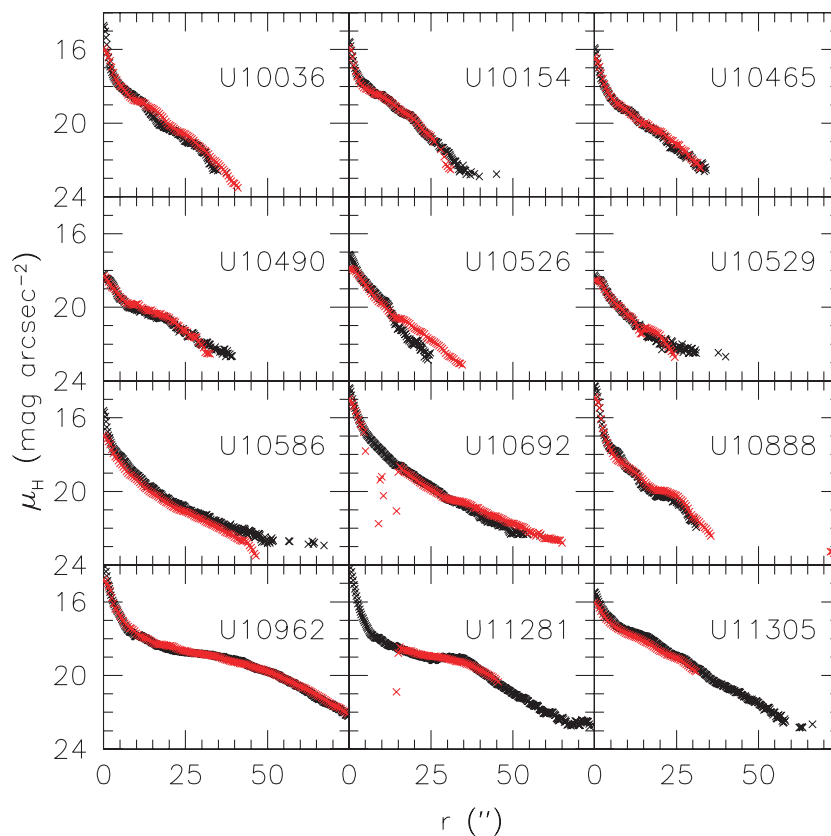**Figure 6.** Comparison of M03 (red) and ULBCam (black) H-band SB profiles. These galaxies, while not members of the Virgo cluster, were observed using ULBCam in order to provide an independent comparison of our calibration and analysis techniques.

fitting, using a generalized non-linear least-squares fitting routine. The ellipticity and position angle, but not the centre, of each elliptical isophote are allowed to vary. The centre is determined by measuring the centroid of the central light distribution with the XVISTA command AXES. Beyond one to two disc scalelengths, the position angle and ellipticity usually settle to constant values. The isophotal solution based on these values is extrapolated to larger radii where the signal-to-noise ratio (S/N) is too low for PROFILE to converge on a unique solution. Adjustments to the ellipticity profile can be made with the XVISTA command, CPROF, to account for abrupt changes due to any non-axisymmetric features. Ellipse fitting to map the radial SB profile requires the galaxy to be slightly (but not fully!) inclined, so that the azimuthal direction is projected on to the plane of the sky. Edge-on galaxies are thus excluded from this procedure. Fortunately, only three galaxies in our sample have inclinations $>80°$; non-parametric structural measures (e.g. effective SB) for those galaxies are still valid.

4.4 Profile depth and signal-to-noise ratios

We calculate the S/N ratio of a SB profile as a function of radius as

$$\frac{S}{N}(r) = \frac{I_t(r)\,\text{pixel}^{-2} \times \sqrt{A_{\text{ell}}}(\text{pixel})}{\sqrt{I_{\text{sky}}}\,\text{pixel}^{-1}}, \tag{1}$$

where the number of pixels (expressed as an area) along each isophote is given by

$$A_{\text{ell}} = 2\pi\sqrt{0.5(a^2 + b^2)}, \tag{2}$$

where a, b are the semimajor and semiminor axes of a given elliptical isophote, $I_t(r)$ is its total SB level (intensity in counts), and I_{sky} is the SB of the sky.

The measurement of I_{sky} was outlined in Section 4.1. According to equation (1), depths of $\sim 23.5\,H$ mag arcsec^{-2} with S/N ~ 3 can be achieved with an exposure time of 480 s (at the 2.2-m UH telescope). For intermediate and low SB galaxies, our exposure times of 960 and 1440 s were determined to yield S/N ~ 3 at SB depths of 24 and 24.5 H mag arcsec^{-2}, respectively. These levels correspond to ~ 4 disc scalelengths for disc galaxies and ~ 5 effective radii for spheroidal systems.

5 NIR DATA QUALITY

While our collection of Virgo cluster galaxy light profiles results from the merging of independent imaging surveys, we have imposed our own uniform analysis methods to the entire data base. Internal errors can be assessed from repeat measurements, and we can compare our extracted light profiles with those from the original authors, whenever available. We can also compare our estimates of empirical quantities such as total luminosity, scale radii and
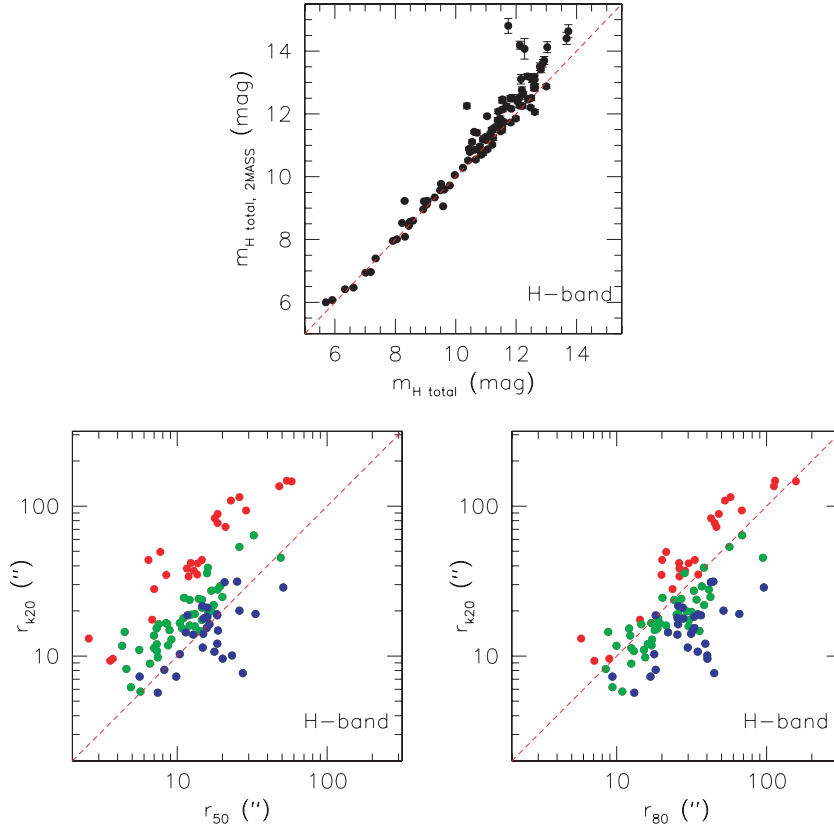

Figure 7. (Top panel) Comparison of the 2MASS total H-band magnitude with our total isophotal H-band magnitude. Up to 12 H mag, the agreement is superb with a typical 1σ deviation of 0.2 mag. The shallower 2MASS is biased towards fainter galaxy magnitudes for $m_H > 12$ mag. (Bottom panels) Comparison of the 2MASS K-band isophotal radius, r_{K20}, measured at the K-band SB of 20 mag arcsec^{-2}, with our own radii, r_{H50} and r_{H80}, which enclose 50 and 80 per cent of the total H-band light, respectively. Modulo the different bandpasses, the scatter is largely due to the different light profile shapes for galaxies with different mean SB. The red points for $\mu_H < 16$ mag arcsec^{-2}, the blue points for $\mu_H > 18$ mag arcsec^{-2} and green points for the galaxies in between make this conclusion very clear. The scatter in the distributions of r_{K20}, r_{H50} or r_{H80}, and SB naturally increases for fainter galaxies.

concentration to those provided with surveys such as 2MASS and SDSS in order to test for systematic differences.

5.1 Independent calibration errors from multiple measurements

We have repeat measurements for three galaxies observed from 2005 to 2007: VCC1614, VCC1516 and VCC1664. We find no variation in the SB profiles over these three epochs, demonstrating the stability of our calibrations over time. Since our calibration of ULBCam data is tied to the 2MASS system, we did not derive extinction coefficients and zero-point corrections for each observing night. However, we can compute relative offsets between the observed and 2MASS magnitudes for several stars in each observed field. The distribution of the photometric offsets shown in Fig. 4 spans 4 yr of observations and a full range of airmasses. The measured width of ∼0.2 *H* mag for this distribution is expected for night-to-night zero-point variations alone (e.g. Courteau 1996).

5.2 Profile comparison with independent measurements

A total of 80 GOLDMine galaxies that satisfy our *Q* criterion (McDonald et al. 2009b) were included in our sample. Original images from GOLDMine's heterogeneous collection of galaxies were kindly provided to us by G. Gavazzi. The average *H*-band SB zero-point offset of ±0.15 mag arcsec^{-2} between our ULBCam and GOLDMine's original light profiles is small enough to justify merg-

ing the two samples into one. However, for complete uniformity, we have recomputed SB profiles for GOLDMine galaxies using our own data reduction techniques outlined earlier. Another motivation for doing so is the desire to have linearly, rather than logarithmically (as in GOLDMine), sampled SB profiles. This exercise also led to more data points in the outer discs, which is relevant for the extrapolation of light profiles to infinity. Fig. 5 shows the overlap of our profiles derived from ULBCam and GOLDMine images for selection of VCC galaxies covering a broad range in luminosity and morphology.

We now compare our calibrated profiles with the fully homogeneous data base of deep *H*-band images of late-type northern spirals by MacArthur et al. (2003; hereafter M03). These *H*-band images of spiral galaxies were collected at the Kitt Peak National Observatory (KPNO) 4-m telescope with the Cryogenic Optical Bench (COB) detector; typical total integration times were 20 min per galaxy. We observed 12 non-Virgo UGC galaxies from M03's sample with ULBCam in 2007 April for comparison. As shown in Fig. 6, the match with M03 is typically very good, with a mean deviation between the two samples of ∼0.1 mag arcsec^{-2}. This comparison with an independent data base reinforces the quality of our data set.

To summarize this section, we have shown that we can merge our *Q* > 0.5 GOLDMine and ULBCam *H*-band SB profiles into one sample with a systematic error <0.15 mag arcsec^{-2}. Because all profiles are calibrated to 2MASS, the 2MASS profiles with *Q* > 0.5 are also naturally integrated into our system. Our entire collection of *H*-band SB profiles is thus self-consistent to within <0.15 mag arcsec^{-2} out to the last measured data point.
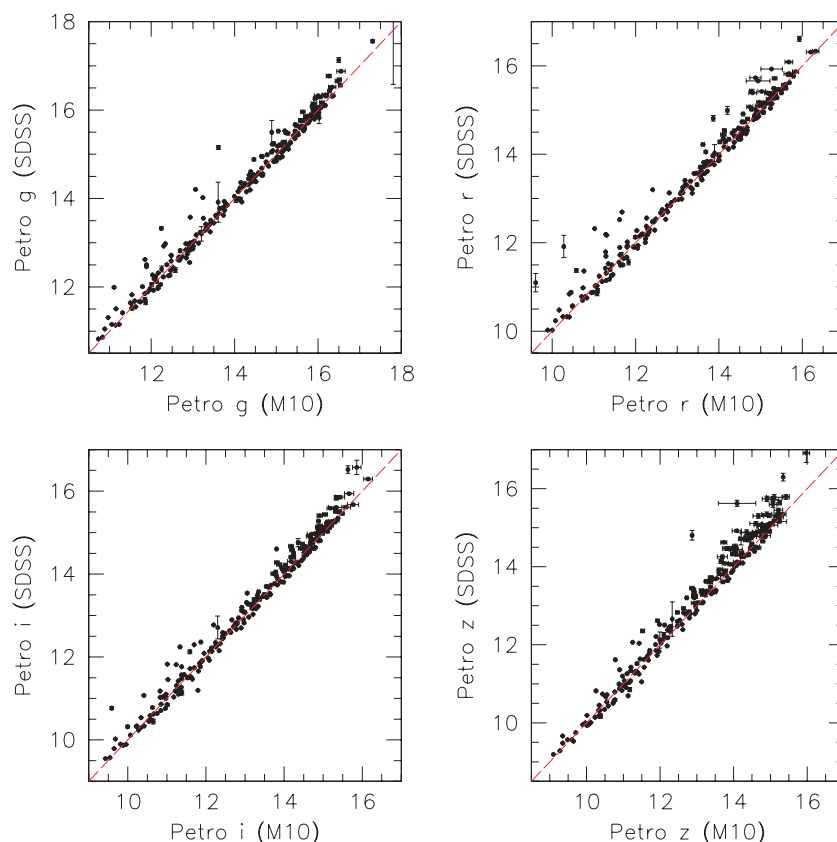

Figure 8. Comparison of available Petrosian magnitudes from the SDSS pipeline and those calculated based on our SB profiles extracted from SDSS images. The red, dashed lines represent the one-to-one relations. These plots confirm that our zero-point calibration, and magnitudes are properly computed.

5.3 Comparison of 2MASS and SDSS data products

We can also compare our well-tested, non-parametric data products, such as the half-light radius and total magnitude, with those provided by automated 2MASS and SDSS pipelines. The upper panel of Fig. 7 shows our total, extrapolated H-band brightnesses versus those provided by 2MASS. The agreement between the two samples for $H < 12$ mag is excellent; however, the shallower 2MASS catalogue is biased for fainter magnitudes. The lower panels of Fig. 7 show our H-band radii against the 2MASS K-band isophotal radius, r_{K20}, measured at the K-band SB level of 20 mag arcsec^{-2}. We compare r_{K20} to two radii, r_{50} and r_{80}, which enclose 50 and 80 per cent of the total H-band light, respectively. Besides the bandpass differences, the scatter in this distribution is largely due to the bias between an absolute metric, r_{K20}, and a relative metric, r_{50} or r_{80}; the former is fixed for any galaxy profile, whereas the latter shifts radially as a function of galaxy profile shape. The two measures thus differ as a function of galaxy mean SB, as shown in Fig. 7; the agreement worsens for $\mu_H > 18$ mag arcsec^{-2}. Overall, for $m_H < 13$ mag and $\mu_H < 18$ mag arcsec^{-2}, the 2MASS total magnitudes and isophotal radii are reliable to within $\sim$0.1 mag and 0.2 dex, respectively.

Before performing a similar comparison with the SDSS data, we must first confirm that we have properly extracted and calibrated these data. To that end, we extract Petrosian magnitudes from our calibrated profiles and compare these to the published

SDSS Petrosian magnitudes (Adelman-McCarthy et al. 2008). For a fair comparison, we use the distributed Petrosian radii and computed the total brightness within a circular aperture of that radius. The results from this analysis, shown in Fig. 8, confirm that we reproduce the published Petrosian magnitudes to within their error for nearly all galaxies. This confirms our proper calibration of the SDSS SB profiles.

A comparison with various SDSS data products is shown in Fig. 9. The top figure shows the SDSS Petrosian r-band magnitude versus our total isophotal r-band magnitude from SDSS images. Many galaxies have Petrosian magnitudes more than 2 mag fainter than ours, likely due to a galaxy misidentification by the SDSS pipeline (see Hall et al., in preparation). The mean $\sim$0.2 mag offset from the one-to-one line for well-behaved systems is simply the reflection of comparing our total magnitudes extrapolated to $r = \infty$ with Petrosian magnitudes which are measured within a finite aperture. The deviation at the bright end is due to the SDSS pipeline 'shredding' of large galaxies (e.g. Panter, Heavens & Jimenez 2004). The large scatter at all magnitudes is most likely due to the misidentification of clumpy, star-forming galaxies into several individual sources. The bottom left-hand panel of Fig. 9 shows the SDSS Petrosian half-light radius, $r_{50,\mathrm{SDSS}}$, against the half-light radius, r_{50}, measured with our own software from SDSS images. The deviation from the one-to-one line is largely due to comparing radii derived from circular (SDSS) apertures versus elliptical apertures, since, at a given radius, a circular aperture will always
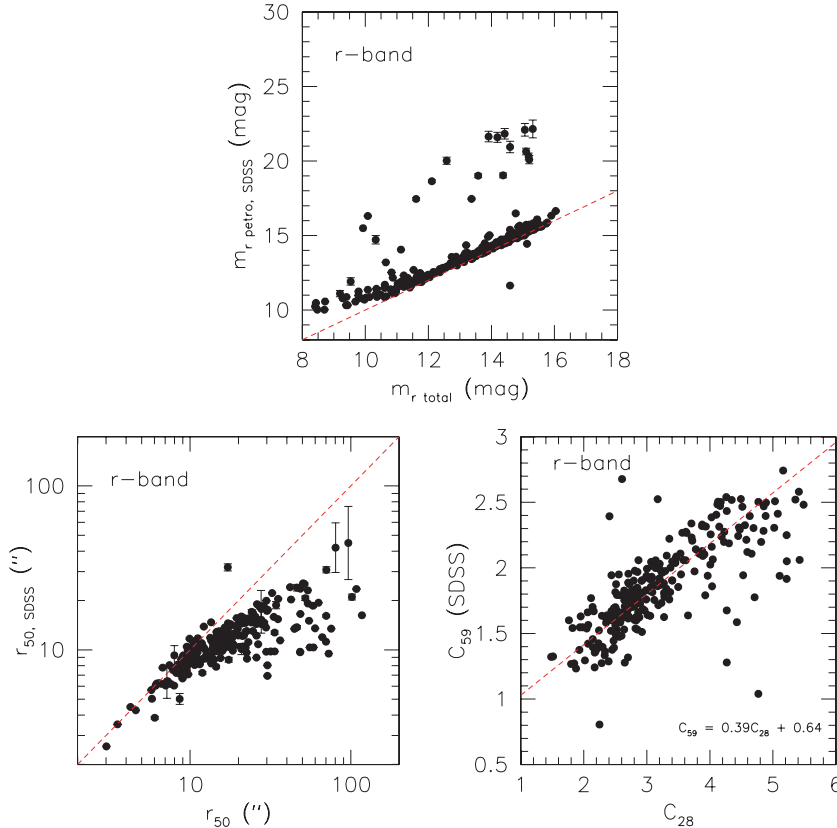

Figure 9. (Top panel) Comparison of the SDSS Petrosian r-band magnitudes with our total isophotal r-band magnitudes from SDSS images. The offset at the bright end is due to the SDSS pipeline 'shredding' large galaxies. The large scatter is also due to SDSS's misidentification of clumpy, star-forming galaxies into multiple sources. (Bottom panels) Left-hand panel: comparison of the SDSS Petrosian r-band half-light radii, $r_{50,\mathrm{SDSS}}$, with the r-band half-light radii, r_{50}, measured with our own software from SDSS images. The deviation from the one-to-one line is largely due to comparing radii derived from circular (SDSS) apertures versus elliptical apertures. Right-hand panel: comparison of SDSS concentration, C_{59}, with our own measure, C_{28}.
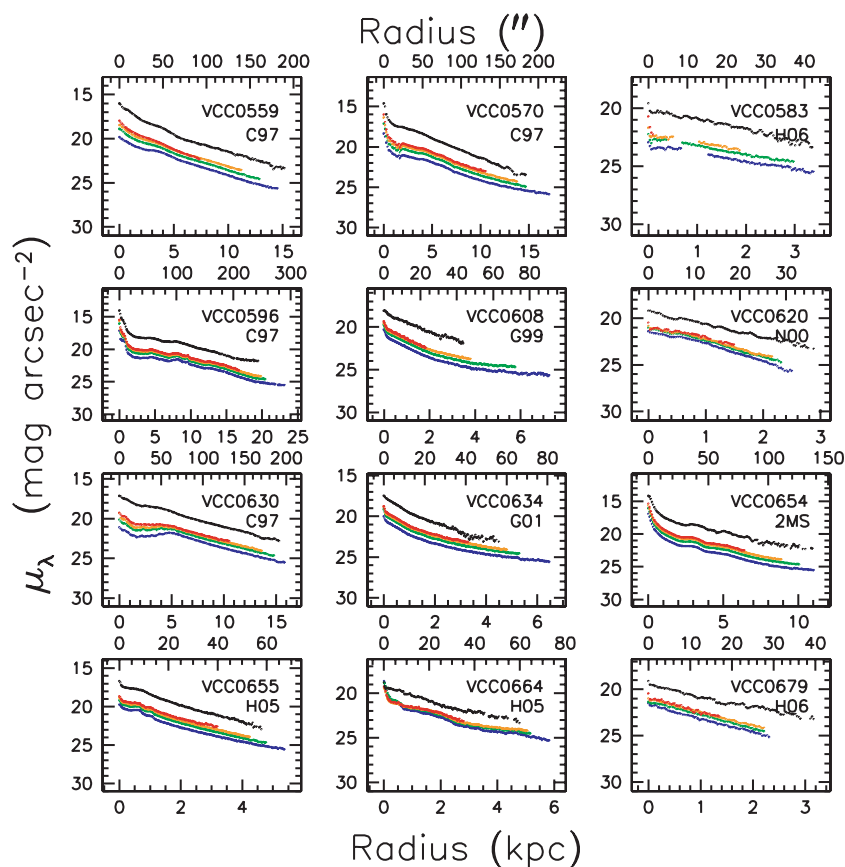
Figure 10. SB profiles for a subset of the 286 galaxies in our sample. The colour coding is as follows: *g* (blue), *r* (green), *i* (orange), *z* (red) and *H* (black). The VCC galaxy name is included in the upper right-hand corner of each window, with the *H*-band data source beneath it. The data source codes are H## (UH 2.2-m ULBCam observations from 2005, 2006, 2007 and 2008), CFH (CFHT WIRCAM), UKT (UKIRT WFCAM), 2MS (2MASS archive). All other codes (C##, N##, T##, G##) refer to data taken from the GOLDMine survey and correspond to the telescope used and year of the observation. (The SB profiles for all 286 galaxies are available online at http://www.astro.queensu.ca/virgo/.)

enclose more flux than an elliptical aperture of the same maximal size.

Finally, the lower right-hand corner of Fig. 9 shows a comparison of our and the SDSS concentration parameter, defined as $C_{XY} = 5\log_{10}(r_Y/r_X)$, where r_X and r_Y contain $X \times 10$ per cent and $Y \times 10$ per cent of the total light of the galaxy. The curvature between the radii seen in the lower left-hand panel of Fig. 9 cancels out to yield a rather linear, albeit noisy, mapping between the two concentrations. The conversion between the two concentration parameters is given by $C_{59} = 0.34C_{28} + 0.71$.

Overall, these comparisons highlight the risks of taking survey data at face value (see also Hall et al. in preparation).

6 SURFACE BRIGHTNESS PROFILES

We show in Fig. 10 the *griz* and *H*-band SB profiles for 12 of the 286 VCC galaxies in our main sample (see http://www.astro.queensu. ca/virgo/ for the full collection). The full morphological range spanned by our sample from blue to red and dwarf to giant is demonstrated by the wide variety of light profile shapes. To demonstrate this, we have computed the average *r*-band SB profile for galaxies in several morphological bins. Fig. 11 shows the differences and similarities between light profiles at all morphological types, normalized at μ_e and r_e. In a plot of $\mu - \mu_e$ versus r/r_e, all SB profiles must pass through the point (1, 0). In each window, we

show the normalized SB profiles of a given morphology, with the mean profile per morphological bin shown in colour. The middle and lower windows to the right show the average SB profiles in each morphological bin interior and exterior to r_e. For $r \lesssim 0.3r_e$, gas-poor (E, S0, Sa) galaxies exhibit classical cuspy bulges, while gas-rich types (Sb, Sc, Sd, dwarf and irregular galaxies) have cored profiles, commonly associated with pseudo-bulges (M03; Kormendy & Kennicutt 2004). For $r \gtrsim 0.3r_e$, the relative shape of the outer profiles can be compared. Both giant and dwarf spheroidal systems (E, dE, S0, dS) have similar shapes, while disc-like systems (Sa–Sd) exhibit a more exponential outer profile.

Similar conclusions are reached if we bin the profiles by concentration rather than morphological type (Fig. 12). The use of a quantitative measure for the concentration yields tighter distributions as opposed to the more subjective morphological classification. There is a natural division for systems with pseudo-bulges ($C < 3.8$) versus those with a classical bulge ($C > 3.8$), as shown by McDonald et al. (2009b).

We find the same results with the *H*-band data, though the *r*-band data are, typically, deeper than at *H* band. The most notable difference is with the depth of the dwarf and irregular galaxy profiles. The average dE, dS and Irr profiles are well defined out to much larger radii at *r* band than at *H* band. Overall, the trends that are present in the mean *H*-band profiles are reproduced at *r* band, suggesting that these mean profiles are robust.
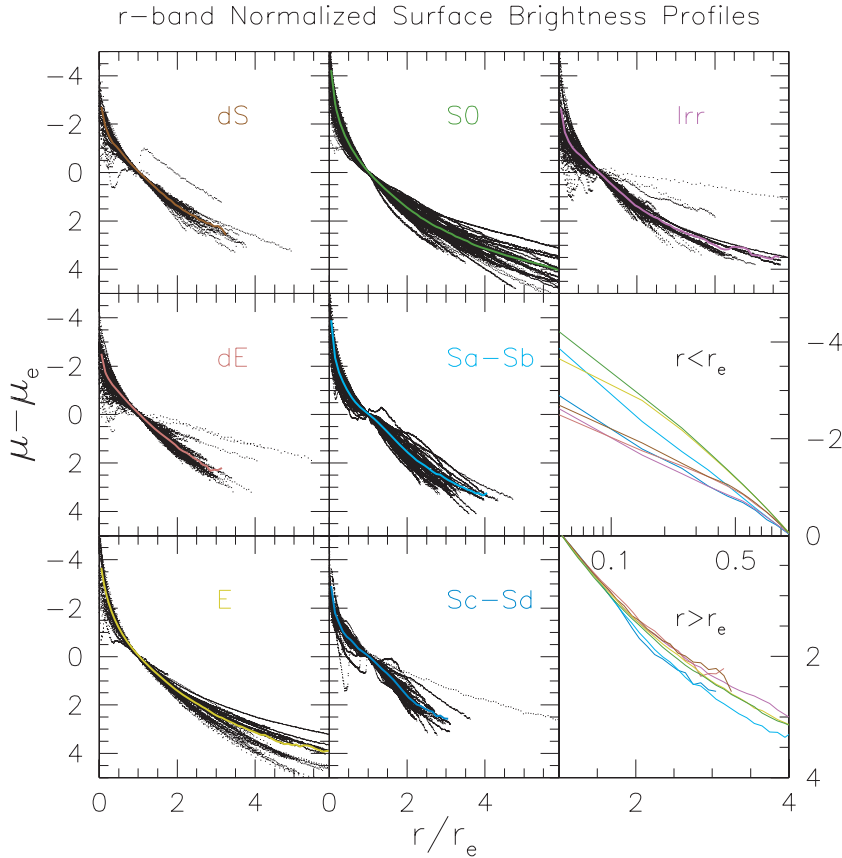
Figure 11. *r*-band SB profiles for our entire sample, rescaled in terms of μ_e and r_e, and binned by morphological classes. Average profiles for each bin are represented by coloured lines. The middle and lower windows in the right-hand panels show the average profiles interior and exterior to r_e.

Whereas Lauer et al. (2007) hinted at a bimodal separation of the central regions of giant and dwarf ellipticals into cuspy and cored profiles, respectively, Côté et al. (2007) showed that the distribution of central profile shapes is a continuum. Côté et al. suggested that a possible selection bias and choice of radius at which the inner slope is measured could explain the differences, showing that a continuum of inner slopes is seen in the comparison of the inner profile slope with a non-parametric parameter such as total luminosity. Our Fig. 12 attests to the continuous distribution of inner slopes when we bin by galaxy concentration (which correlates with total luminosity). Thus, a dichotomy between cuspy and cored profiles is only seen if profiles are binned by morphology; a continuous distribution prevails with a more physically motivated binning criterion such as concentration.

7 GALAXY STRUCTURAL PARAMETERS

In order to determine the contribution of the bulge and disc components to the total galaxy light, we have performed 1D bulge–disc decompositions on the full sample of Virgo cluster galaxies following the techniques described in McDonald et al. (2009a). Due to the 1D nature of these decompositions, we are unable to fully account for non-axisymmetric components such as bars and ovals. These components will necessarily be added to either the bulge or the disc light, adding a degree of uncertainty to these fits. Ideally, one should use a 2D decomposition code such as GIM2D (Simard et al. 2002), BUDDA (de Souza, Gadotti & dos Anjos 2004) or GALFIT (Peng et al. 2010) so that non-axisymmetric features can be prop-

erly modelled. For further discussion of the relative merits of 1D and 2D bulge–disc decompositions, see M03. While 2D decompositions can reduce some of the inherent uncertainty in 1D model parameters, differences between 1D and 2D values are at the 10–20 per cent level. We proceed with our 1D approach here; our 2D decompositions will be presented elsewhere. We describe the salient features of this method below.

Our bulge model uses a generalized Sérsic function (Sérsic 1968) with three free parameters: an effective (or half-light) radius, r_e, the SB at that radius, I_e, and a shape parameter, n. For the special case of $n = 1$, the Sérsic function reduces to a simple exponential. The disc light is modelled with an exponential function described by two free parameters: a disc central SB, I_0, and a disc scalelength, h. The bulge and disc models are convolved with the Moffat (1969) function to simulate the effects of seeing on the intrinsic light profile of a galaxy.

For spiral and irregular galaxies (S0–Sd, Irr) we model the SB profile with a combination of a Sérsic bulge and exponential disc. If the inclusion of the bulge component does not sufficiently improve the fit quality (i.e. Sd or Irr galaxies), the software will discard it and fit an exponential function alone in an attempt to decrease the degrees of freedom and, thus, minimize the reduced χ^2. Since spheroidal galaxies (E, dE, dS) may or may not have a disc, we also attempt to model the profile with a single Sérsic. Once again, if the absence of a disc component increases the goodness of fit, the software will automatically discard this component of the model. The fit minimization uses brightnesses in magnitude (not counts), and the lowest global value of the χ^2 per degree of freedom determines the best fit.

r−band Normalized Surface Brightness Profiles
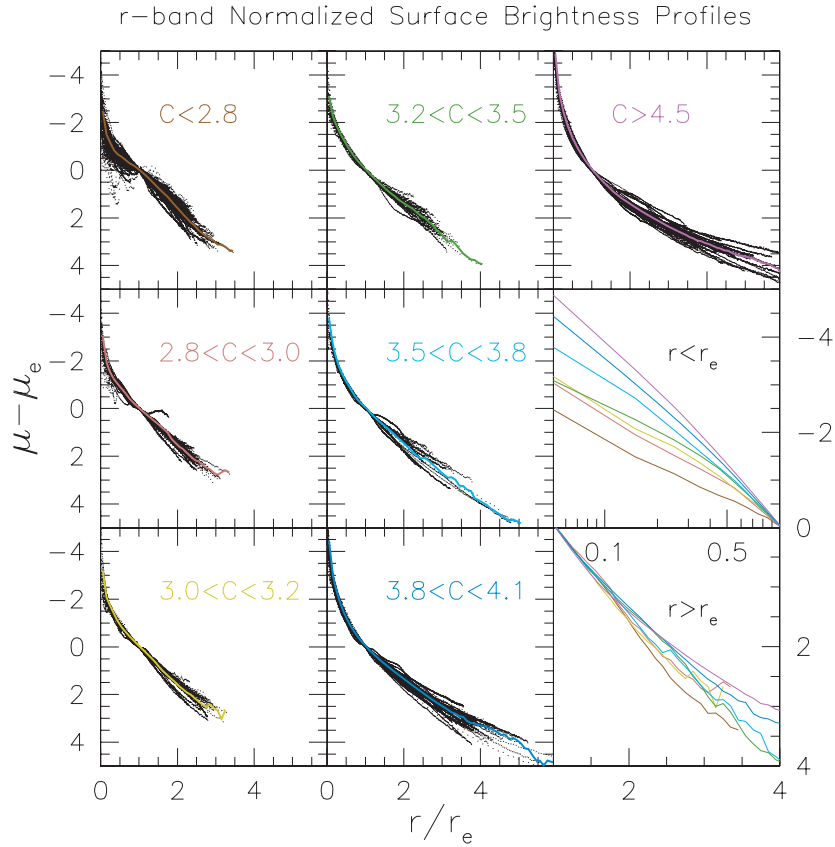
Figure 12. *r*-band SB profiles for our entire sample, rescaled in terms of μ_e and r_e, and binned by concentration. Average profiles for each bin are represented by coloured lines. The middle and lower windows in the right-hand panels show the average profiles interior and exterior to r_e.
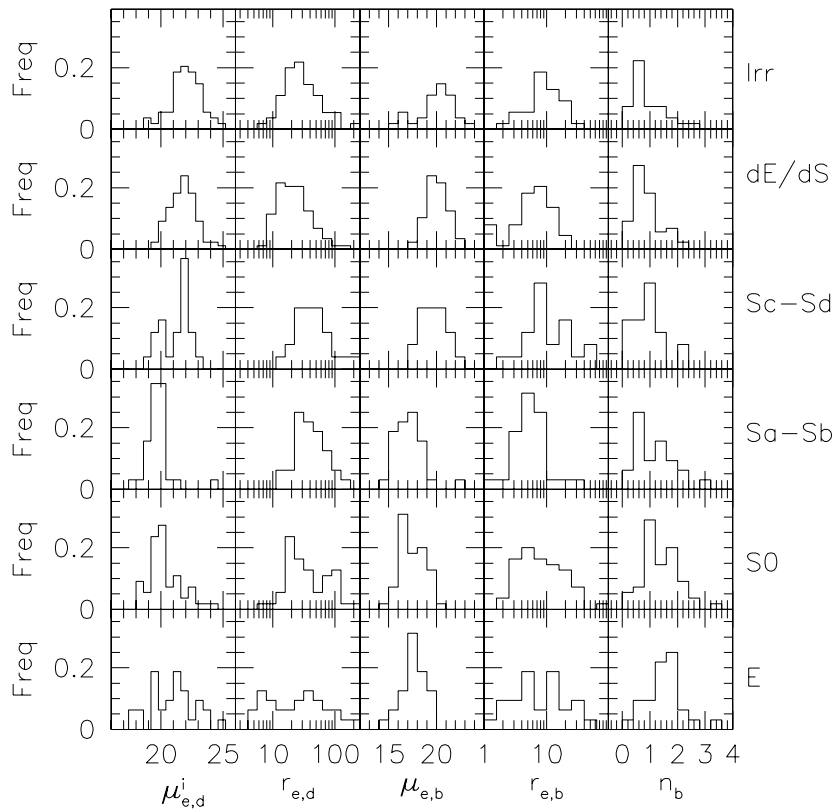
Figure 13. Distribution of *H*-band structural parameters from bulge–disc decompositions for Virgo galaxies sorted into six different morphological bins.

Our model decomposition can also account for the presence of a nucleus, here modelled by a seeing-convolved delta function at $r = 0$ (one additional free parameter, m_{nuc}), as well as spiral arms, which are modelled by a smooth increase in brightness above the underlying disc. We find that the addition of a nuclear component reduces the need for high-n bulges, yielding an average shape parameter of $n \sim 1$. These additional features increase the degrees of freedom and, thus, are only applied for obvious cases.

Non-parametric structural measurements, such as the total magnitude (extrapolated from the last data point to infinity), the effective radius and SB, and galaxy light concentration, were computed for all 286 galaxies in each of the five bands. These measurements are nearly independent of the bulge–disc model decompositions, relying only on the fit in order to determine the amount of galaxy light beyond the last data point (typically <0.2 mag). The fact that these parameters are independent of any model (i.e. no assumption that a galaxy profile can be separated into components) makes them most useful for galaxy structure studies. The effective radius, r_e, is defined as the radius which encloses half the total light, while the effective SB is the SB at this radius, $\mu_e = \mu(r_e)$. We compute the concentration parameter, C_{28}, as in Section 5.3.

The parametric and non-parametric structural measurements for our 286 VCC galaxies in the *griz* and H bands are provided online at the Centre de Données astronomiques de Strasbourg (CDS) website (http://cds.u-strasbg.fr/) and our private website (http://www.astro.queensu.ca/virgo/). For spiral galaxies with well-defined bulges and discs (i.e. Sa–Sb), we find typical r-band errors

on our fitting parameters of $\Delta\mu_{e,d} = 0.1$ mag arcsec^{-2}, $\Delta\mu_{e,b} = 0.2$ mag arcsec^{-2}, $\Delta r_{e,d} = 3$ per cent, $\Delta r_{e,b} = 15$ per cent and $\Delta n_b = 0.3$. These uncertainties are similar to those reported by M03, who relied on similar techniques. For irregular or poorly sampled systems, these uncertainties can increase by as much as an order of magnitude. The distribution of the H-band parametric quantities is shown in Fig. 13 for different morphological bins. This figure clearly shows the disc SB bimodality discovered by TV97 and confirmed by McDonald et al. (2009a,b). These distributions are meant to be compared to galaxy formation models.

8 TABLES OF MEDIAN STRUCTURAL PARAMETERS

We provide in Table 1 the median and standard deviation of the four non-parametric parameters (total magnitude, effective SB, effective radius and concentration) as a function of morphology and bandpass. This table shows the variation of galaxy structural parameters with wavelength and morphology, as well as the spread of each parameter within a given morphological/wavelength bin. For instance, there is a substantial range in elliptical galaxy brightnesses, as expected from the bimodal distribution of elliptical SBs (McDonald et al. 2009b), and a clear division of galaxies into cuspy ($C_{28} \sim 4.0$) and disc-like ($C_{28} \sim 2.8$) galaxies, also as reported by McDonald et al. (2009b). Additionally, Table 1 shows that disc galaxies have, on average, effective radii that are twice as large as spheroidal galaxies, regardless of SB or colour.

Table 1. Median and standard deviation of Virgo cluster galaxy non-parametric structural quantities for different morphologies and bandpasses.

Parameter	Morphology	g	r	i	z	H
$m_T{}^a$	E	13.5(1.8)	12.9(1.8)	12.4(1.8)	12.7(1.9)	10.6(2.2)
(mag)	S0	12.5(1.3)	11.6(1.4)	11.2(1.4)	11.0(1.5)	9.3(1.6)
	Sa–Sb	12.1(1.2)	11.5(1.3)	11.1(1.3)	10.9(1.3)	9.0(1.5)
	Sc–Sd	13.3(1.3)	12.7(1.5)	12.6(1.4)	12.4(1.5)	9.9(1.8)
	dE	15.3(0.9)	14.7(0.8)	14.4(0.9)	14.2(1.3)	12.5(0.9)
	dS	14.7(0.5)	14.1(0.6)	13.8(0.6)	13.6(0.7)	11.7(0.9)
	Irr	14.9(1.3)	14.3(1.4)	14.0(1.5)	13.7(1.5)	12.3(1.6)
$\mu_e{}^b$	E	22.0(1.4)	21.2(1.5)	20.9(1.5)	20.5(1.4)	18.3(1.5)
(mag arcsec^{-2})	S0	22.3(0.9)	21.5(1.0)	21.1(1.0)	20.8(1.0)	18.9(1.1)
	Sa–Sb	22.8(0.7)	22.2(0.7)	21.8(0.7)	21.5(0.7)	19.5(0.7)
	Sc–Sd	23.5(0.7)	23.0(0.7)	22.7(0.7)	22.3(0.7)	20.6(1.0)
	dE	24.1(0.7)	23.4(0.7)	23.1(0.8)	22.6(0.7)	21.1(0.9)
	dS	23.8(0.9)	23.2(0.8)	22.9(0.8)	22.5(0.8)	20.6(0.8)
	Irr	23.7(1.0)	23.3(1.1)	23.1(1.1)	22.6(1.1)	21.3(1.3)
$r_e{}^c$	E	1.1(0.8)	1.1(0.8)	1.1(0.9)	1.0(0.7)	0.9(1.1)
(kpc)	S0	1.7(0.9)	1.8(0.9)	1.7(0.9)	1.6(0.8)	1.4(1.0)
	Sa–Sb	2.6(1.6)	2.5(1.5)	2.9(1.4)	2.5(1.4)	2.5(2.0)
	Sc–Sd	2.4(1.8)	2.4(1.7)	2.4(1.5)	2.3(1.4)	2.2(2.4)
	dE	1.3(0.5)	1.3(0.5)	1.2(0.5)	1.0(0.8)	1.2(0.5)
	dS	1.2(0.6)	1.2(0.5)	1.2(0.5)	1.2(0.5)	1.1(0.5)
	Irr	1.4(0.7)	1.4(0.7)	1.5(0.8)	1.3(0.7)	1.3(0.8)
$C_{28}{}^d$	E	3.8(0.7)	3.9(0.7)	4.0(0.7)	3.8(1.0)	3.8(0.7)
	S0	4.0(0.8)	4.1(0.8)	4.1(0.8)	4.2(0.8)	4.0(0.9)
	Sa–Sb	3.1(0.7)	3.2(0.7)	3.2(0.7)	3.3(0.7)	3.4(0.7)
	Sc–Sd	2.6(0.4)	2.5(0.5)	2.8(0.5)	2.7(0.6)	2.8(0.4)
	dE	2.9(0.6)	3.0(0.6)	2.9(0.6)	2.7(0.5)	2.9(0.5)
	dS	3.3(0.4)	3.3(0.4)	3.2(0.4)	2.9(0.4)	3.3(0.6)
	Irr	2.7(0.8)	2.7(0.8)	2.6(0.7)	2.5(0.7)	2.6(0.7)

[a]Total apparent magnitude extrapolated to $r = \infty$ (mag); [b]effective SB (mag arcsec^{-2}); [c]effective radius (kpc); [d]concentration: $C_{28} = 5\log_{10}(r_{80}/r_{20})$.

Table 2. Median and standard deviation of Virgo cluster galaxy parametric structural parameters from bulge–disc decompositions for different morphologies and bandpasses.

Parameter	Morphology	g	r	i	z	H
n^a	E[b]	2.4(1.1)	2.6(1.0)	2.3(1.0)	2.2(1.4)	2.1(0.9)
	E[c]	1.4(0.6)	1.5(0.5)	1.5(0.6)	1.3(0.7)	1.5(0.7)
	S0	1.4(0.6)	1.4(0.5)	1.4(0.6)	1.3(0.6)	1.2(0.7)
	Sa–Sb	1.2(0.7)	1.2(0.6)	1.4(0.6)	1.2(0.7)	1.0(0.6)
	Sc–Sd	0.5(0.3)	0.7(0.5)	0.6(0.4)	0.6(0.4)	0.8(0.5)
	dE/dS	0.9(0.3)	0.9(0.4)	0.9(0.4)	0.8(0.4)	0.8(0.5)
	Irr	0.6(0.6)	0.8(0.6)	0.7(0.5)	0.5(0.5)	0.7(0.6)
$\mu_{e,b}{}^d$	E[b]	22.7(1.4)	21.7(1.4)	21.4(1.4)	21.3(1.5)	18.7(0.9)
(mag arcsec^{-2})	E[c]	21.0(1.4)	20.5(1.4)	20.2(1.4)	19.8(1.6)	17.5(1.3)
	S0	20.6(1.3)	20.0(1.3)	19.4(1.4)	19.2(1.5)	17.2(1.3)
	Sa–Sb	21.2(1.2)	20.5(1.2)	20.3(1.4)	19.9(1.4)	17.6(1.5)
	Sc–Sd	22.6(1.5)	21.9(0.9)	21.6(1.0)	21.4(1.2)	19.7(1.4)
	dE/dS	23.0(0.9)	22.6(0.9)	22.2(1.0)	21.9(0.9)	20.0(1.1)
	Irr	22.6(1.4)	22.1(1.5)	21.8(1.6)	21.0(1.7)	20.2(1.8)
$r_{e,b}{}^e$	E[b]	1.7(2.3)	1.6(2.0)	1.5(2.0)	1.5(3.2)	1.3(2.0)
(kpc)	E[c]	0.6(0.4)	0.6(0.3)	0.6(0.3)	0.6(0.3)	0.7(0.9)
	S0	0.8(0.6)	0.8(0.6)	0.6(0.7)	0.6(0.6)	0.6(0.9)
	Sa–Sb	0.5(1.4)	0.6(0.6)	0.6(0.8)	0.6(0.7)	0.5(0.6)
	Sc–Sd	0.5(0.4)	0.4(0.4)	0.6(0.6)	0.6(0.5)	0.7(1.1)
	dE/dS	0.6(0.4)	0.6(0.3)	0.6(0.3)	0.5(0.3)	0.5(0.4)
	Irr	0.6(0.4)	0.8(0.5)	0.8(0.4)	0.4(0.3)	0.8(0.5)
$\mu_{e,d}{}^f$	E[c]	23.8(1.6)	23.3(1.6)	22.7(1.6)	22.3(1.6)	20.9(1.8)
(mag arcsec^{-2})	S0	22.9(1.5)	22.3(1.3)	21.9(1.2)	21.3(1.4)	19.6(1.5)
	Sa–Sb	22.6(1.3)	22.0(0.9)	21.6(1.1)	21.3(1.1)	18.9(1.1)
	Sc–Sd	22.9(0.8)	22.4(0.9)	22.1(1.1)	21.9(0.8)	20.5(1.4)
	dE/dS	24.3(1.0)	23.7(0.9)	23.4(0.9)	22.9(0.9)	21.4(1.0)
	Irr	23.8(1.2)	23.4(1.1)	23.2(1.1)	22.6(0.9)	21.4(1.3)
$r_{e,d}{}^g$	E[c]	2.4(2.3)	2.4(2.6)	2.4(2.4)	2.1(2.5)	2.5(9.1)
(kpc)	S0	3.3(4.0)	3.4(3.5)	3.0(5.0)	2.5(5.0)	2.9(7.5)
	Sa–Sb	3.7(3.6)	3.4(2.2)	3.9(2.0)	3.3(2.7)	3.3(2.6)
	Sc–Sd	2.6(2.7)	2.7(2.5)	2.8(2.5)	2.9(2.1)	3.0(10.7)
	dE/dS	1.9(1.8)	1.9(1.8)	1.9(1.4)	1.8(2.3)	1.8(1.8)
	Irr	2.2(1.8)	2.1(2.3)	2.4(1.6)	2.0(1.2)	2.2(3.0)

[a]Sérsic n parameter; [b]elliptical galaxy light profile fit with single Sersic function; [c]elliptical galaxy light profile fit with Sérsic + exponential functions; [d]bulge effective SB in units of mag arcsec^{-2}; [e]bulge effective radius in units of kpc; [f]disc effective SB in units of mag arcsec^{-2}; [g]disc effective radius in units of kpc.

Table 2 gives the median and standard deviation of five parametric quantities from 1D bulge–disc decompositions. This includes three bulge parameters: $\mu_{e,b}$, $r_{e,b}$, n and the two disc parameters: $\mu_{e,d}$ and $r_{e,d}$. This table shows the variation of bulge and disc structural parameters as a function of colour and morphology. We find that the 'typical' bulge shape is indeed exponential (e.g. Courteau, de Jong & Broeils 1996; M03) and that the light profile of a typical elliptical galaxy is well fitted by a single Sérsic index of $n \sim 2$. No Virgo galaxy spheroid requires $n > 3$. Furthermore, the decomposition of elliptical galaxy light profiles requires the addition of a disc component for ~ 70 per cent of our sample. These discs tend to have low SB, with average brightnesses similar to Sc–Sd galaxies, but typically have scalelengths twice as large. Finally, we find that the typical spiral galaxy disc has a half-light radius $\sim 5 \times$ larger than that of the bulge.

Tables 1 and 2 offer a wealth of information about the structural parameters of galaxies across the Hubble sequence and over a range of wavelengths. An extensive discussion of these trends is found in McDonald et al. (2009b). These tables ought to provide a valuable compendium of galaxy structural properties for theoretical investigations of galaxies as well as a much needed foil for comparisons with high-redshift galaxy samples.

9 SUMMARY

We have presented the results of a NIR survey, supplemented with optical imaging from the SDSS, of 286 morphologically diverse Virgo cluster galaxies. Our NIR images come from various sources including archival H-band data from the 2MASS and GOLDMine archives and new H-band data for 171 galaxies from the UH 2.2-m telescope, CFHT and UKIRT. These NIR data have been carefully calibrated, yielding a photometric accuracy of ~ 0.1 mag arcsec^{-2} over the entire sample. Both the new and archival data were analysed in a homogeneous manner using our own software for uniformity. For each galaxy in our sample, we have extracted g, r, i, z, H SB profiles yielding a deep, multiwavelength collection of surface photometry. Full bulge–disc decompositions were performed in each of the five wavebands for all 286 VCC galaxies. We also provide the average structural parameters for galaxies in various morphological bins, offering a most valuable benchmark for comparison against theoretical investigations of galaxies as well as high-redshift galaxy samples. This data base has recently been utilized in studies of galaxy structural parameters by McDonald et al. (2009b) and stellar populations by Prochaska et al. (2011) and Roediger et al. (2010). The galaxy light profiles and results of bulge–disc decompositions

are available online at the CDS website (http://cds.u-strasbg.fr/) and our own website (http://www.astro.queensu.ca/virgo/).

REFERENCES

Adelman-McCarthy J. K. et al., 2008, ApJS, 175, 297
Baldry I. K., Glazebrook K., Brinkmann J., Ivezić Ž., Lupton R. H., Nichol R. C., Szalay A. S., 2004, ApJ, 600, 681
Balogh M. L., Baldry I. K., Nichol R., Miller C., Bower R., Glazebrook K., 2004, ApJ, 615, L101
Bell E. F., de Blok W. J. G., 2000, MNRAS, 311, 668
Bell E. F., McIntosh D. H., Katz N., Weinberg M. D., 2003, ApJS, 149, 289
Binggeli B., Sandage A., Tammann G. A., 1985, AJ, 90, 1681 (VCC)
Blanton M. R. et al., 2003, ApJ, 594, 186
Brinchmann J., Charlot S., White S. D. M., Tremonti C., Kauffmann G., Heckman T., Brinkmann J., 2004, MNRAS, 351, 1151
Côté P. et al., 2007, ApJ, 671, 1456
Courteau S., 1996, ApJS, 103, 363
Courteau S., de Jong R. S., Broeils A. H., 1996, ApJ, 457, 73
Courteau S., Dutton A. A., van den Bosch F. C., MacArthur L. A., Dekel A., McIntosh D. H., Dale D. A., 2007, ApJ, 671, 203
de Jong R. S., 1996, A&A, 313, 45
de Souza R. E., Gadotti D. A., dos Anjos S., 2004, ApJS, 153, 411D
Gavazzi G., Pierini D., Baffa C., Lisi F., Hunt L. K., Randone I., Boselli A., 1996, A&AS, 120, 521
Gavazzi G., Boselli A., Donati A., Franzetti P., Scodeggio M., 2003, A&A, 400, 451
Hall D. N. B., Luppino G., Hodapp K. W., Garnett J. D., Loose M., Zandian M., 2004, in Garnett J. D., Beletic J. W., eds, Proc. SPIE, Vol. 5499, Optical and Infrared Detectors for Astronomy. SPIE, Bellingham, p. 1
Hambly N. C. et al., 2008, MNRAS, 384, 637
Kauffmann G. et al., 2003, MNRAS, 341, 33
Kirby E., Jerjen H., Ryder S., Driver S., 2008, AJ, 136, 1866
Kormendy J., Kennicutt R. C., Jr, 2004, ARA&A, 42, 603
Lauer T. R. et al., 2007, ApJ, 664, 226L
Lawrence A. et al., 2007, MNRAS, 379, 1599
MacArthur L. A., Courteau S., Holtzman J. A., 2003, ApJ, 582, 689 (M03)
McDonald M., Courteau S., Tully R. B., 2009a, MNRAS, 393, 628
McDonald M., Courteau S., Tully R. B., 2009b, MNRAS, 394, 2022
Mei S. et al., 2007, ApJ, 655, 144
Meurer G. R. et al., 2002, The 2002 HST Calibration Workshop: Hubble after the Installation of the ACS and the NICMOS Cooling System. STSI, Baltimore, p. 65
Moffat A. F. J., 1969, A&A, 3, 455
Panter B., Heavens A. F., Jimenez R., 2004, MNRAS, 355, 764
Peng C. Y., Ho L. C., Impey C. D., Rix H.-W., 2010, AJ, 139, 2097P
Prochaska C. L. C., Courteau S., McDonald M., Rose J. A., 2011, MNRAS, 412, 423
Puget P. et al., 2004, Proc. SPIE, 5492, 978
Roediger J. C., Courteau S., MacArthur L. A., McDonald M., 2010, (arXiv:1011.3511)
Sandage A., Binggeli B., Tammann G. A., 1985, AJ, 90, 1759S
Sérsic J. L., 1968, Atlas de Galaxies Australes. Observatorio Astronomico, Cordoba
Simard L. et al., 2002, ApJS, 142, 1S
Skrutskie M. F. et al., 2006, AJ, 131, 1163
Strateva I. et al., 2001, AJ, 122, 1861
Tully R. B., Verheijen M. A. W., 1997, ApJ, 484, 145 (TV97)

This paper has been typeset from a TEX/LATEX file prepared by the author.